Titel/Title: Oxygen Droplet Combustion in Hydrogen under Microgravity Conditions

Autor*innen/Author(s): Florian Meyer, Christian Eigenbrod, Volker Wagner, Wolfgang Paa, James C. Hermanson, Shion Ando and Marc Avila

Veröffentlichungsversion/Published version: Postprint

Publikationsform/Type of publication: Artikel/Aufsatz

Zusätzliche Informationen/Additional information:

Corresponding author: florian.meyer@zarm.uni-bremen.de, Florian Meyer, Am Fallturm 2, 28359 Bremen, Germany

Oxygen Droplet Combustion in Hydrogen under Microgravity Conditions

Florian Meyer[1], Christian Eigenbrod[1], Volker Wagner[2], Wolfgang Paa[2], James C. Hermanson[3], Shion Ando[4] and Marc Avila[1]*

[1]*University of Bremen, Center of Applied Space Technology and Microgravity (ZARM), Am Fallturm 2, 28359 Bremen, Germany*

[2]*Leibniz-Institute of Photonic Technology, Albert-Einstein-Str. 9, 07745 Jena, Germany*

[3]*University of Washington, William E. Boeing Dept. of Aeronautics & Astronautics, 3940 Benton Lane NE, Seattle, WA 98195, United States*

[4]*Kyushu University, Department of Mechanical Engineering, 744 Motooka Nishi-ku, Fukuoka 819-0395, Japan*

*Corresponding author: florian.meyer@zarm.uni-bremen.de

Florian Meyer, Am Fallturm 2, 28359 Bremen, Germany

Abstract

The combustion of single liquid oxygen droplets in gaseous hydrogen is investigated experimentally under microgravity conditions to shed light on spray combustion processes in rocket engines. Using a drop tower apparatus, experiments are performed varying the ambient pressure between 0.1-5.7 MPa, which corresponds to a reduced pressure of oxygen p_r between 0.02-1.12. The combustion is investigated using high-speed shadowgraph imaging to track the droplet shape and OH-chemiluminescence to identify the flame zone. At low pressures ($p_r < 0.15$), the droplet shape is found to change significantly during combustion likely due to the formation of a water ice layer around the droplet. Small jets of oxygen appear to break out of this ice layer, leading to an observed increase in linear and angular momentum of the droplet. At higher pressures, the visible effect of ice formation near the droplet surface decreases. The combustion process at different pressures in the subcritical and the supercritical regime is compared and discussed. The pressure has a limited influence on the flame standoff ratio, whereas it influences the burning rate constant substantially. Specifically, the experimental data suggest a maximum of the burning rate constant near the critical pressure, which is consistent with several experiments on hydrocarbon droplet combustion.

Keywords: Droplet combustion, Rocket combustion, Liquid oxygen, Hydrogen, Microgravity

1. Introduction

Spray combustion is widely employed in many engineering applications and is characterized by the multiple superposition and nonlinearly coupled interactions of individual sub-processes, including liquid jet disruption, droplet formation and vaporization, ignition, and combustion. In the field of rocket propulsion, the hydrogen-oxygen system exhibits the highest specific impulse and is often used as a propellant combination. In this case, numerous small oxygen ligaments, lumps, and droplets vaporize and combust in the rocket combustion chamber to generate thrust. Even state-of-the-art simulations in modern supercomputers are not able to reproduce spray combustion in full detail. Therefore, simplified models are typically employed to describe and predict the processes in rocket combustion chambers [1-4]. In order to model the overall spray combustion process, it is necessary to represent the aforementioned sub-processes as simply and precisely as possible. In this study, the combustion of a single liquid oxygen droplet in hydrogen is investigated. This is the most basic configuration to understand the fundamentals of droplet vaporization, combustion, flame front location and water vapor production.

Our goal is to achieve a fundamental understanding of hydrogen-oxygen droplet combustion as a basis for spray combustion in rocket engines. The experiments presented here are used to determine key combustion parameters such as droplet lifetime, flame standoff ratio, and droplet regression rate and to study combustion effects such as the condensation/freezing of water near the droplet. Our measurements help to understand the underlying physical and chemical processes and support model development as well as the validation of (sub-)models.

One of the first single droplet combustion experiments was performed by Godsave [5] in 1953. He investigated burning droplets of several fuels with shadowgraph imaging and found that the droplet lifetime is proportional to the square of the droplet diameter. His work and the work of Spalding [6] led to the formulation of the *classical theory* (later referred to as d^2-law). To enable comparison with theoretical (spherically symmetric) droplet combustion models, convection must be eliminated, since otherwise the influence of natural convection on the droplet burning rate is too severe to be neglected. For this reason, Kumagai & Isoda [7] performed the first systematic droplet combustion experiments under microgravity conditions back in 1957. Under quiescent microgravity conditions natural and forced convection are suppressed. As a consequence, single droplets and their corresponding flames are spherical and can be accurately modelled with a single spatial dimension (the droplet radius). At the same time, microgravity conditions allow for comparatively large droplets (millimeter length scale), which enables the application of sophisticated diagnostics. Considerable progress has been made since the pioneering work of Kumagai & Isoda and microgravity has been repeatedly shown to be an appropriate and powerful tool to understand the influence of diffusion and convection in combustion processes. Examples include the demonstration aboard the ISS that large droplets undergo self-extinction and then continue to burn in the cool-flame

regime [8], or studies on the interaction between neighboring droplets during ignition [9] and combustion [10].

To the best of our knowledge, the microgravity approach has so far not been applied to the combustion of single oxygen droplets vaporizing and burning in a gaseous hydrogen environment. In general, liquid oxygen and hydrogen are difficult to handle and require stringent safety measures. As a result, the experimental database on oxygen droplet combustion or vaporization, even under normal gravity conditions (hereafter 1g), is very limited. In one basic 1g study, Yang *et al.* [11] examined the vaporization of liquid oxygen under subcritical and supercritical conditions. Using a pool-like configuration in a convective helium environment with a fixed flow velocity of 0.2 cm/s and a fixed temperature of 290 K, they found an almost linear increase in vaporization rate with increasing pressure, ranging from 0.5 to 6.9 MPa (reduced pressure $p_r = 0.1$ to 1.4). In another experimental study under 1g conditions, Chesneau *et al.* [12] studied the vaporization of single oxygen droplets in stagnant air, nitrogen, and helium at room temperature. They also found a significant increase in the vaporization rate with increasing pressure. To compare these findings with simplified numerical predictions they applied a buoyancy correction based on the Grashof number. This correction compensates for gravitational effects and results in a reduced increase in vaporization rate with increasing pressure between 0.1 and 3 MPa.

In contrast to the very limited experimental studies, there have been many numerical studies on hydrogen-oxygen droplet vaporization and combustion. One of the first numerical investigations of the vaporization of an oxygen droplet under subcritical and supercritical conditions and high ambient temperatures was carried out by Delplanque & Sirignano [13]. In addition to unsteady effects at subcritical pressure conditions, such as transient droplet heating, they also studied vaporization effects near the critical point. They found that the fractional difference between the droplet surface and droplet core temperature is larger compared to hexane droplets and remains significant during most of the droplet lifetime. In the supercritical pressure regime, neglecting gas-phase solubility in the droplet results in significant underestimation of the critical mixing temperature, which is reached very quickly by the droplet surface at hot ambient temperature [13]. Yang *et al.* [14] studied the pressure effects on oxygen vaporization in hydrogen environments. They found that the droplet lifetime decreases with increasing pressure in the subcritical regime, and also in the supercritical regime, before the droplet lifetime then increases slightly from a pressure of 8 MPa ($p_r = 1.6$) on. Although they discussed different effects at subcritical and supercritical conditions, they had no clear explanation for the minimum droplet lifetime at this pressure. Haldenwang *et al.* [15] found qualitatively similar results in their study and termed this phenomenon, which occurs at high temperatures close to the critical pressure, "transcritical minimum". However, they found that the chosen definition of the droplet surface under supercritical conditions (based on temperature or mass fraction) strongly affects the appearance of this phenomenon. Yang [16] summarized several studies on vaporization as well as combustion and attributed the increase in vaporization rate in the subcritical regime to the decrease

in the enthalpy of vaporization. By contrast, in the supercritical regime, the enthalpy of vaporization drops to zero and the increase in thermal diffusivity near the droplet surface causes the droplet lifetime to decrease, according to his study. Oschwald *et al.* [17] studied the phase behavior of the hydrogen-oxygen system in equilibrium. The solubility of the gas in the liquid can increase substantially at elevated pressures, and it becomes necessary to consider the critical properties of a mixture. For pressures above the critical point, critical lines of mixing define the thermodynamic state. Below the critical mixing temperature, phase equilibrium between the liquid and gas exists. Above this temperature, the mixture exhibits supercritical behavior. They pointed out that the critical mixing temperature for the binary hydrogen-oxygen system decreases with increasing pressure [17]. Lafon *et al.* [18, 19] also studied the vaporization effects of an oxygen droplet in a hot hydrogen atmosphere, including the effects of the Dufour and Soret cross-diffusion terms [19]. Their model results showed a steady increase in vaporization rate and a corresponding decrease in droplet lifetime with increasing pressure even above the critical pressure of oxygen. In the supercritical regime, the droplet lifetime was seen to decrease more rapidly with increasing pressure [18, 19]. This trend depends on the ambient temperature and the definition of the droplet surface. The effects of the Dufour and Soret cross-diffusion terms were estimated to have a negligible effect on the vaporization behavior of the droplet [19].

Daou *et al.* [20] performed a numerical study to investigate the combustion of an oxygen droplet in a quiescent hydrogen environment under supercritical conditions with detailed chemistry. They studied ignition, flame structure and addressed the effect of ambient pressure. They found that for a droplet diameter of 50 μm, the combustion time increased by less than 4% with an increase in pressure from 10 to 20 MPa. They compared this with experimental results of Sato *et al.* [21] who also found a slight increase in combustion lifetime for hydrocarbon droplets in the supercritical regime.

For hydrocarbons, the data set on droplet combustion is much more extensive than for the case of liquid oxygen. The reported pressure effects in the subcritical and supercritical regime for hydrocarbons can be used for comparison with the results of the current study of hydrogen-oxygen combustion. For example, Sato *et al.* [21] studied the pressure effects on the combustion of n-octane droplets under microgravity. They found that the combustion lifetime decreases significantly with increasing pressure. In the immediate vicinity of the critical pressure, however, the combustion lifetime reaches a minimum and then slightly increases again in the supercritical regime. In another study, Sato [22] found that in addition to n-octane, also n-heptane, n-decane, n-hexadecane, ethanol, and methanol showed a similar pattern of changes in burning rate with pressure. The burning rate constant, as determined from the d^2-law, was seen to increase with increasing ambient pressure and to reach a maximum near the critical pressure of the fuel. Beyond the critical pressure, the burning rate decreased slightly. Sato also pointed out that the combustion lifetime and the droplet lifetime may be different due to residual vaporized fuel that needs additional time to burn [22]. These results are in agreement with the experimental data of Faeth *et al.* [23] and Vieille *et al.* [24] who

burned several hydrocarbon as well as ethanol and methanol droplets in microgravity. In a review study, Givler & Abraham [25] concluded in 1996 that the available data indicate a minimum combustion lifetime occurring exactly at the critical pressure for all hydrocarbons, even though there is a lack of substantial experimental data to support this. More recently, Okai *et al.* [26] studied the pressure effects of single droplets and droplet pairs of methanol under µg conditions. In addition to the effects of the neighboring droplets, they found that the droplet lifetime for single droplets decreased monotonically over the entire pressure range investigated ($p_r = 0.01$ to 1.11). Other comprehensive studies were performed, e.g., by Dietrich *et al.* [27] on n-decane droplets and by Mikami *et al.* [28] on mixtures of n-heptane and n-hexadecane droplets both under µg conditions.

These findings for the pressure effects of burning hydrocarbon fuels are in contrast to studies [11, 13, 18, 19] on pure oxygen vaporization mentioned earlier, which showed a further decrease in droplet lifetime even in the transition from subcritical to supercritical ambient pressure conditions. However, some numerical studies [14, 15] have identified a "transcritical minimum" and found a minimum droplet lifetime in the supercritical pressure regime. To summarize, the lack of experimental data on single oxygen droplet combustion does not yet allow clear conclusions to be drawn on the effect of ambient pressure on oxygen combustion lifetime. Determining this effect is a goal of the current study.

Another issue discussed in the literature is the possible condensation or freezing of water vapor near or on the cold oxygen droplet surface. Powell [29] attempted to experimentally simulate the condensation of water vapor on the oxygen droplet surface using liquid nitrogen as a substitute. However, with the diagnostic technique used, he was only able to detect small ice or water particles in the wakes of the liquid nitrogen droplets and not on the droplet surface. Litchford & Jeng [30] studied this phenomenon numerically for the vaporization of oxygen droplets at subcritical pressures. They pointed out the importance of considering not only the ice formation on the surface during vaporization, but also any remaining ice particles after the droplet vanishes. Lafon *et al.* also reported the condensation or freezing of water vapor near the oxygen droplet surface in several numerical studies [18, 19, 31]. They assumed that the nucleation process takes place almost instantaneously and condensed water is subjected to thermophoretic and viscous forces. They also assumed that water or ice particles are continuously blown away from the droplet surface by the gaseous flow of oxygen induced by droplet vaporization. Therefore, the ice layer was assumed to be very thin since the high diffusivity of hydrogen leads to a flame zone close to the droplet surface, resulting in a steep local temperature gradient. Another goal of this study is to investigate the formation and the effect of this ice layer.

In the current study, combustion experiments of suspended oxygen droplets in a quiescent cryogenic hydrogen atmosphere (77 K) were conducted under microgravity conditions in the subcritical and supercritical pressure regime for oxygen ranging from 0.1 to 5.7 MPa ($p_r = 0.02$ to 1.12). For this purpose, a drop tower apparatus [32] was used to generate, suspend, and combust single oxygen droplets with a

nominal diameter of ~0.7 mm. Optical diagnostics were employed to visualize the flame size and position as well as the droplet diameter regression to answer fundamental questions about the burning rate, droplet/combustion lifetime, and flame standoff ratio. Of particular interest were the pressure effects during the transition from the subcritical to the supercritical pressure regime and the possible formation of condensed or frozen water vapor during combustion. To illustrate these basic combustion effects, a schematic diagram of the expected combustion process is shown in **Fig. 1**.

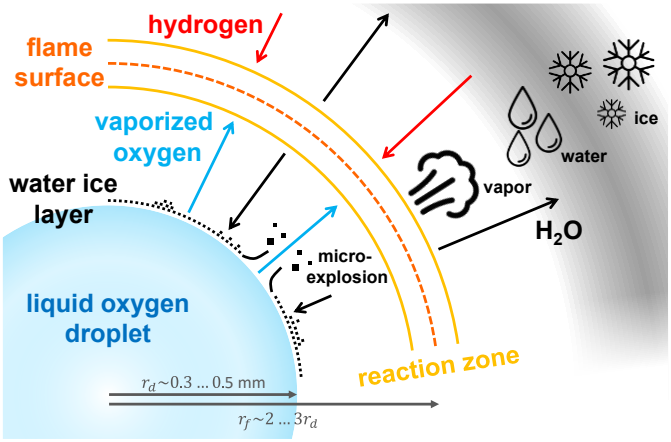

Fig. 1. Schematic overview of the expected combustion process.

After ignition, a flame is formed, which is purely diffusion-driven under microgravity conditions. The stoichiometric position of the flame is relatively close to the droplet surface due to the high diffusion velocity of hydrogen. As a result, the liquid oxygen is rapidly heated and vaporized, leading to short combustion lifetimes. During combustion, water vapor forms in the reaction zone and is transported both outward and inward. Outside the hot flame, the temperature drops to the ambient temperature of the combustion chamber of 77 K. Consequently, the resultant water vapor condenses and freezes. The same occurs when the water vapor within the flame reaches the cold droplet surface, which can lead to the formation of an ice layer around the droplet, as assumed in the literature [18, 19, 29-31]. Oxygen jets could break through this ice layer, resulting in local micro-explosions. This happens with a quite similar background with burning alcohol droplets where the exhaust water outmatches the droplet's blowing and accumulates in the droplet's surface as it is soluble in alcohol. The layer in this case forms a vaporization barrier as it has a higher boiling temperature than pure alcohol, which leads to micro-explosions [26, 33].

2. Experimental setup and diagnostics

The experimental drop tower setup used for these experiments is described in great detail in a previous publication [32]. The setup is briefly summarized here with a focus on the suspender design, the optical

measurement methods, and the evaluation techniques including the image processing. A simplified schematic setup of the experiment and the diagnostics used for this study is shown in **Fig. 2**.

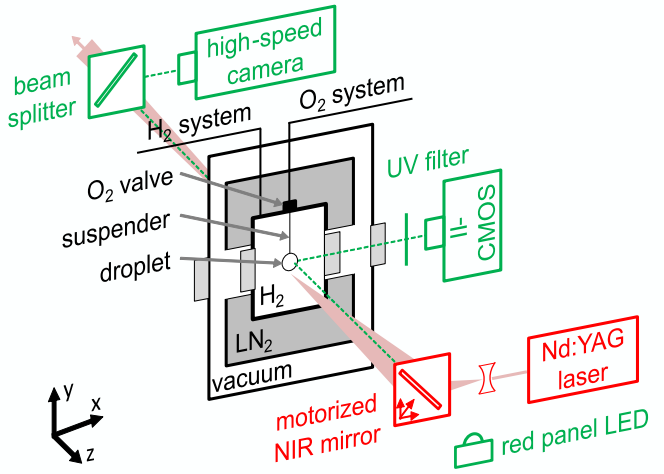

Fig. 2. Simplified schematic overview of the experimental setup. Red: ignition system with illustrated laser beam path (z-axis). Green: diagnostics with indicated optical beam paths (dashed lines, x/z-axis).

The main component of the setup is the cryogenic combustion chamber (diameter: 43 mm, height: 60 mm), which is connected to a pressure-regulated hydrogen supply (H_2 system) and to the oxygen supply (O_2 system) via a valve in the combustion chamber lid. The entire combustion chamber is surrounded by a container filled with liquid nitrogen (LN_2). The liquid nitrogen container is in turn surrounded by a vacuum container to thermally insulate the combustion chamber. All three containers are separated by orthogonally arranged fused silica windows (x/z-axis) to provide optical access from four sides (clear diameter of 15 mm). The droplet is generated inside the combustion chamber just before the free-fall phase in the drop tower. For this purpose, the oxygen supply valve on the combustion chamber lid is opened. Due to cooling with liquid nitrogen at 77 K, the oxygen gas condenses in the lower part of the oxygen line and in the oxygen supply valve. The resulting liquid oxygen is slowly drawn into the combustion chamber by venting hydrogen. Inside the combustion chamber, a fused silica suspender is mounted into the combustion chamber lid (**Fig. 3**). This material and the dimensions of the lower suspender part were chosen to withstand the high thermal stress during combustion. The upper part of the suspender is a tube, which is thermally drawn into a tapered needle with a diameter of 0.2 mm. Still under 1g conditions, the liquid oxygen is drawn into the suspender, passes through a lateral hole to the outside, and then runs downwards to the suspender tip, which consists of a sphere with a diameter of 0.5 mm. This technique allows a single droplet to be separated from the liquid column inside the suspender and to remain suspended at the tip of suspender in the center of the combustion chamber. The ignition of the droplet during the free-fall phase is achieved by a laser-induced plasma breakdown. For this purpose, a Nd:YAG laser is directed into the combustion chamber and focused below the droplet (**Fig. 2**, red components).

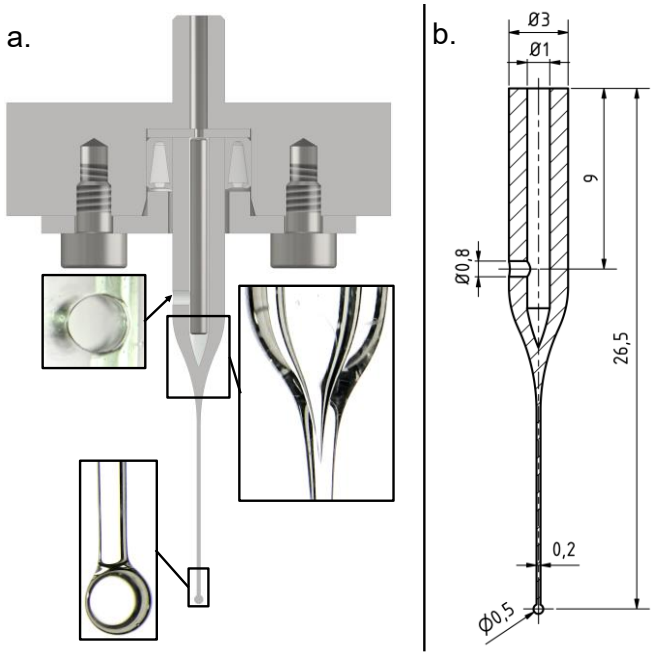

Fig. 3. a. Suspender holder and fused silica suspender: cross-sectional CAD view with three embedded actual suspender images (tip of suspender without droplet). b. Suspender cross-section with dimensions in mm.

Two primary diagnostic systems were used in this study, as shown in **Fig. 2** (green components). Shadowgraph imaging was utilized as the primary diagnostic system to determine the droplet diameter as well as the droplet shape during combustion. In addition, direct hydroxyl (OH) chemiluminescence imaging was employed to determine the position and size of the flame. For shadowgraphy, a high-speed camera system (Photron MC2) with a resolution of 16.1 µm/px at a frame rate of 2000 fps was used in combination with a red area LED with a diffuser as the light source. The camera system was synchronized with the ignition laser to ensure that the ignition spark is recorded to allow the position of the spark to be verified in each case. For the OH-chemiluminescence imaging, a double intensified camera (II-CMOS) with a resolution of 27.0 µm/px at 1600 fps was used. This camera system (Lambert HiCAM 500 ST) recorded the OH-chemiluminescence at a wavelength of 308 nm and was protected from the bright flame by an ultraviolet filter (UG11, Schott). The shadowgraph and OH-chemiluminescence diagnostics were arranged orthogonally to allow for simultaneous imaging.

For the evaluation of the acquired images, the existing MATLAB tool [32] was further developed to determine the droplet diameter and the flame zone diameter. Since the droplet shape can deviate significantly from the spherical shape under certain conditions, as discussed below, a multi-stage evaluation process was used to calculate the equivalent droplet diameter. For this purpose, a circle detection algorithm, the Hough transformation [34], was first used to determine a preliminary center point and the preliminary diameter of the droplet. Starting from this center point, all surrounding pixels within the preliminary detected circle were evaluated according to a threshold relative to the actual background brightness and were

determined whether the pixels belonged to the droplet or the background. Thus, non-circular shapes could also be correctly detected and an equivalent droplet diameter could be calculated based on the sum of all droplet pixels. To evaluate the droplet shape, the centroid of the identified droplet pixels was calculated and used as a center point to determine the shortest and the longest dimension line of the droplet within a resolution of 1 degree, i.e., 360 lines. For an exact circular shape (resulting in a spherical droplet shape), the ratio between the longest and the shortest line, defined here as R, would be equal to unity. Thus, the droplet shape ratio R is used as a two-dimensional measure of the deviation from a spherical shape, as shown in **Fig. 4a-b**. For the OH-chemiluminescence images, the Hough transformation was applied directly to determine the diameter of the spherical flame, as shown for different pressures in **Fig. 4c-d**.

The automatic detection of the size of the droplet and the flame zone was verified manually for certain time steps of each experiment. For eight experiments (at $p_r > 0.3$ and at $p_r = 0.15$), the images were evaluated semi-automatically, since the superposition by the outer water cloud layer led to errors in the fully automatic determination. For this purpose, the droplet zone was defined manually for every fifth image, so that the algorithm could calculate the droplet shape ratio on this basis. Due to the changes in brightness during the combustion caused by the water cloud, there could be minimal fluctuations in the diameter determination using this method. However, the measurement uncertainties of the optical measurement methods appear to have been dominated by the non-spherical droplet shape at low pressures. The deviation of the droplet shape ratio from unity can give an indication at which time the measurement uncertainty is increased, but the complex shape of the droplet could not be measured unambiguously using only one camera. In contrast, the determination of droplet lifetime and initial droplet diameter was not significantly affected by these two effects.

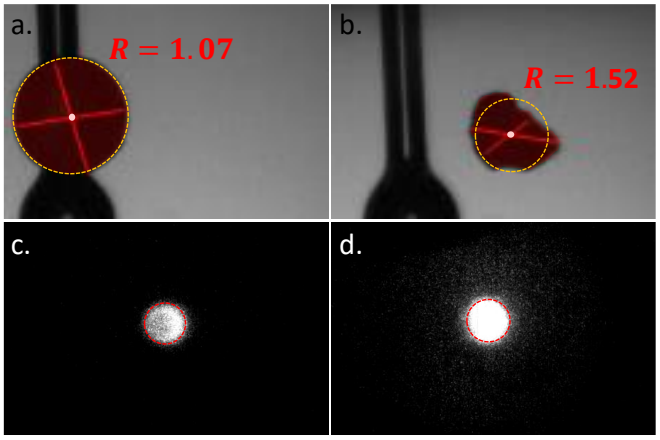

Fig. 4. Examples of MATLAB droplet and flame calculations: a-b. Droplet shape ratio R calculation at $p_r = 0.02$ (red colored area: identified droplet pixels; white dot: calculated centroid; red lines: longest and shortest droplet dimension through centroid; yellow dashed line: detected equivalent diameter). c-d. Flame diameter detection at $p_r = 0.04$ and $p_r = 0.09$, respectively (red dashed line: detected flame diameter).

3. Results and discussion

In this study, nineteen drop tower experiments were evaluated. For all experiments, the microgravity time was 4.7 s with a residual acceleration of the order of 10^{-6} g (hence microgravity). The initial droplet diameters were 0.72 mm in average with a standard deviation of 0.1 mm and the ambient hydrogen pressure was varied between 0.1 to 5.7 MPa, corresponding to reduced pressures p_r of 0.02 to 1.12 (critical pressure of oxygen, $p_{c,O_2} = 5.043$ MPa; critical temperature of oxygen, $T_{c,O_2} = 154.58$ K).

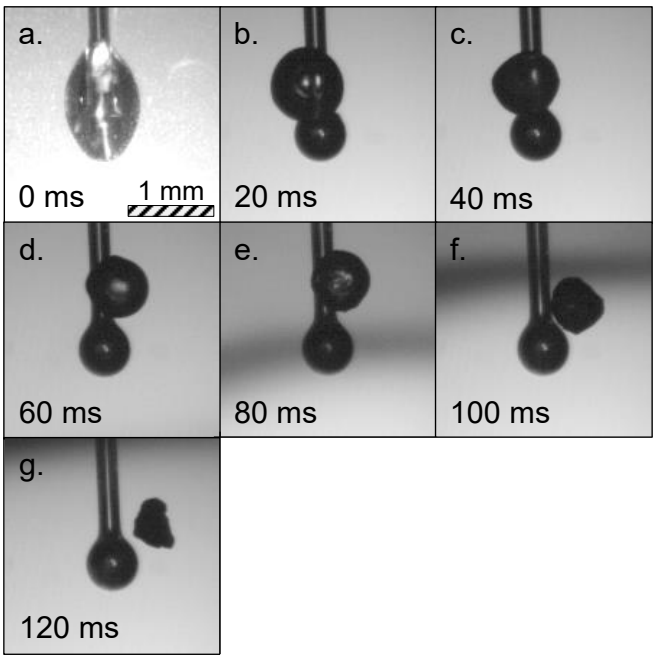

Fig. 5. a.-g. High-speed shadowgraph sequence of LOX droplet regression at an ambient pressure of $p_r = 0.02$. Ignition occurred at 0 ms (a). The video file is provided as supplementary material.

The first feature discussed here is the detachment of the burning droplet shortly after ignition, which occurred in all experiments and has never been reported before in experiments with suspended hydrocarbon droplets. A shadowgraph sequence of the combustion process at a reduced pressure $p_r = 0.02$ is shown in **Fig. 5**. After droplet generation, liquid oxygen accumulated not only around the spherical suspender tip, but also along the suspender needle due to the wetting behavior of liquid oxygen on fused silica. This accumulation was enhanced by the shape of the suspender, as the suspender tip had to be relatively large to ensure that the falling liquid remained on the suspender during droplet generation under 1g conditions. Incidentally, it was also observed that this droplet shape in a very similar way on a sapphire suspender. Hydrocarbon droplets also show this shape, but less pronounced. As a result, the lower part of the spherical suspender tip was covered only with a thin liquid film. The elongated, ellipsoidal shape of the droplet during droplet generation under 1g conditions apparently became intensified under microgravity conditions as the gravitational pull on the liquid vanished, see **Fig. 5a**. After ignition by the laser-induced plasma breakdown

slightly below the suspender tip, the droplet was evidently deformed by the resulting pressure wave. It could be that this pressure wave and the ignition in close proximity to the suspender caused the thin liquid film to dry and rupture. As a result, the vaporizing liquid that sloshed back and oscillated for a few milliseconds no longer spread completely around the suspender but contracted to an approximate spherical shape above the suspender sphere. The droplet then migrated upward along the spherical tip of the suspender (**Fig. 5b-c**) until it ultimately detached from the suspender approximately 50 ms after ignition (**Fig. 5d**). In experiments with hydrocarbons, a transition from the elongated, wetting shape to an approximate spherical shape is also observed after ignition, but without subsequent detachment. Another difference, that may play a decisive role here, is the required close proximity of the ignition spark to the droplet surface in order to ignite the rapidly diffusing ignitable mixture around the vaporizing oxygen droplet. Although the ignition limits in the hydrogen-oxygen system are much further apart than in the hydrocarbon-air system, the high diffusion rate of hydrogen in oxygen causes both the rich and lean ignition limit to be located in a very small area in the immediate vicinity of the droplet surface. Therefore, despite wider ignition limits, the ignition spark must be positioned closer to the droplet than in the hydrocarbon-air system. While burning, the droplet remained free-floating near the suspender, as shown in **Fig. 5d-g**. Complete detachment was indicated by the transition from rapid translational motions to smooth motions and rotations, as well as minor oscillations of the droplet, as can be seen in the shadowgraph video (supplementary material).

For cases without ignition, i.e., with an ignition spark that initiated a pressure wave but did not ignite the mixture around the droplet, the droplet deformed, but immediately returned to its original position, re-enclosing the suspender sphere, and resuming its elongated, ellipsoidal shape due to the wetting of the suspender needle above the suspender sphere (**Fig. 5a**). This suggests that the heating due to the presence of the flame significantly changed the wetting properties of the burning droplet. Without ignition, the surface temperature of the droplet was low and the adhesive force appear to have dominated over the surface tension. However, after ignition, the surface temperature was increased and the adhesive force became weak, resulting in the detachment of the droplet from the suspender. Although also the surface tension was decreased at high temperatures, this effect was limited and the droplet kept a spherical shape after the detachment from the suspender, as expected under microgravity conditions.

For the nineteen experiments evaluated in what follows, the time to complete droplet detachment from the suspender was 15 to 50 ms after ignition and depended on the initial diameter of the droplet as well as on the position of the ignition spark. The detachment of the droplet was not anticipated and it complicated the evaluation of the optical diagnostic results. However, the separation of the droplet from the suspender served to protect the suspender from the hot hydrogen-oxygen flame and the simultaneous high oxygen concentration in the immediate vicinity of the droplet, which in combination would substantially stress the material. Due to the free-floating of the droplets after droplet detachment, the suspender did not affect the shape of the droplet and also the flame was not noticeably disturbed by the suspender. Only in one

experiment did the flame heat the suspender close to the end of the droplet lifetime to the extent that the suspender tip started to glow (see shadowgraph video in the supplementary material). With this exception, it was therefore assumed that the flame was at a sufficient distance from the suspender and was not affected. In any case, in order to compare all experiments in a consistent manner and to minimize the effect of the suspender, the experimental results were evaluated only after the complete droplet detachment from the suspender.

As expected in **Fig. 1**, a water cloud consisting of condensed or frozen water is formed in all experiments and is in fact clearly visible as an evolving sphere/ring around the burning droplet, as can be seen in **Fig. 6** or in **Fig. 12**. The diameter of this ring decreases and the cloud becomes opaque with increasing pressure (**Fig. 12**). The cloud rings slowly shift radially outward during combustion and become blurred as more water is produced.

The shadowgraph sequence of the combustion at a reduced pressure of 0.02 (**Fig. 5**) shows that the shape of the oxygen droplet changed substantially during the combustion process. At the time of the detachment from the suspender (**Fig. 5d**), the droplet had a round and smooth shape. As the combustion progressed (**Fig. 5e-g**), structures increasingly formed on the visible surface, making the surface less transparent and irregular in shape. The change in shape is assumed to result from the inhomogeneous formation of ice structures close to the droplet surface due to the low droplet temperature, despite of the large temperature difference between the hot flame and the cold droplet surface. In fact, the formation of this ice layer around the burning droplet has been predicted in many studies [18, 19, 29-31]. In addition, the droplet began to rotate and translate irregularly, with the rotation and translation becoming more pronounced as the droplet mass decreased. Remaining ice particles after the burning process, as predicted by Litchford & Jeng [30], were observed in all experiments and can be seen in **Fig. 6**. The translational acceleration of the remaining ice particles at the end of combustion and the increasing, irregular rotation of the droplet suggest that the ice layer was subject to small micro-explosions. This effect can be clearly seen in **Fig. 6**, where after complete consumption of the liquid oxygen a remaining ice fragment breaks through the water cloud around the droplet at the end of combustion. Small oxygen-vapor jets issuing from pores in the irregular ice surface could therefore be sources of linear and angular momentum, which may have led to the observed translation and rotation of the droplet. Whether the ice layer was on the surface or only near the surface cannot be determined unambiguously from the shadowgraph images, since the ice formation obscured the view of the actual droplet surface. On the one hand, we assume that thermophoretic forces pulled the ice particles toward the cold droplet surface, as reported in the literature [19]. On the other hand, the Stefan flow of the vaporizing droplet likely counteracted this movement. More detailed studies of the ice layer and its formation are planned for further experiments.

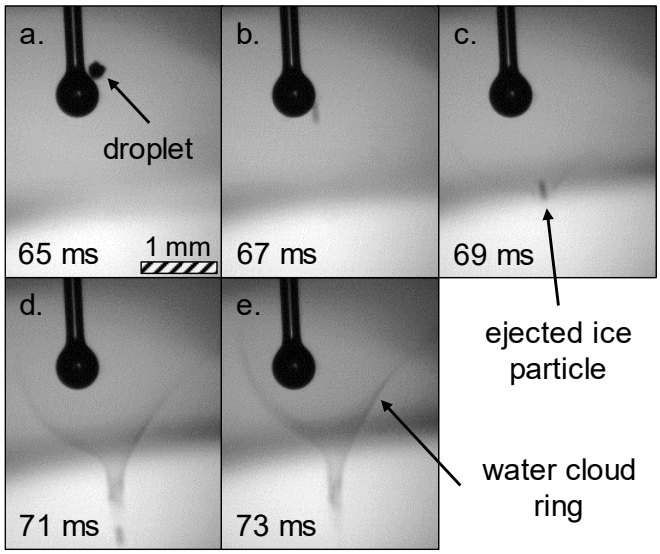

Fig. 6. a.-e. High-speed shadowgraph sequence of remaining ice particle breaking through the inner water cloud ring due to micro-explosions at the end of combustion (all liquid consumed) at $p_r = 0.04$. Ignition occurred at 0 ms.

In the upper panels of **Fig. 7** the dimensionless diameter squared $(d/d_0)^2$, where d_0 is the initial droplet diameter after separation from the suspender, as a function of the normalized time t/t_1, where t_1 is the observed time of droplet disappearance, is shown. For $\mathrm{p_r} = 0.02$ (**Fig. 7a**), after the droplet detaches from the suspender, at $t/t_1 = 0$, the dimensionless equivalent diameter initially remains essentially constant until $t/t_1 = 0.4$. Subsequently, the observed droplet regression deviates significantly from the linear course expected for quasi-steady combustion, possibly because of the formation and growth of an ice layer. In the bottom panels of **Fig. 7** the droplet shape ratio R is shown, calculated from the longest and the shortest dimension of the droplet. For $\mathrm{p_r} = 0.02$ (**Fig. 7a**), the droplet shape ratio strongly deviates from unity, which indicates a non-spherical shape of the droplet and of the surrounding ice layer. Hence, three-dimensional effects evidently affect the determination of the equivalent droplet/ice shell diameter in the subsequent evolution. For combustion at higher pressures (**Fig. 7b-c**), the droplet regression approximately follows the liner course, indicating quasi-steady combustion. The deviation in **Fig. 7b**. after $t/t_1 = 0.8$ is evidently caused by the growth of ice structures on the surface, which is well visible in the shadowgraph images (supplementary material) due to the glow of the suspender tip. The droplet shape ratio $R \approx 1$ shows for these experiments that the droplet shape was approximately spherical during most of the burning time.

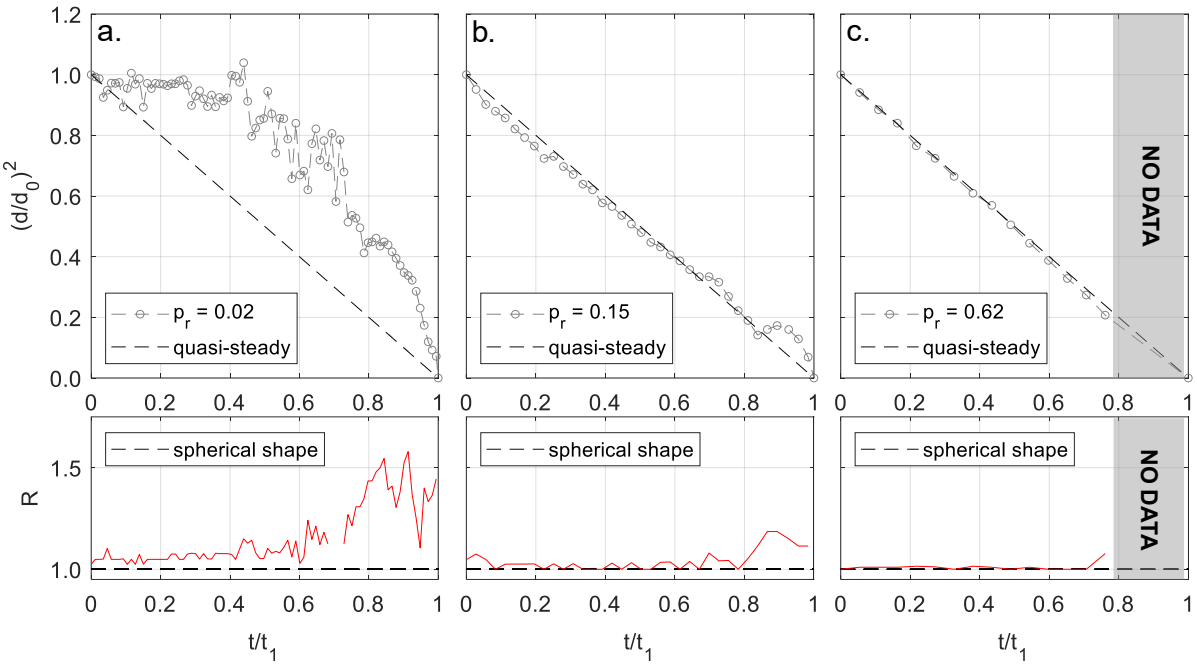

Fig. 7. Dimensionless time evolution of dimensionless droplet diameter (top) and droplet shape ratio R (bottom) for combustions at $p_r = 0.02$ (a), $p_r = 0.15$ (b), and $p_r = 0.62$ (c).

The time evolution of the measured flame diameter f and the flame standoff ratio f/d are shown in **Fig. 8**. For $\mathrm{p_r} = 0.02$ (**Fig. 8a**), the actual flame diameter appears to decrease somewhat for dimensionless times less than $t/t_1 = 0.4$. Subsequently, the flame zone diameter remains constant for a while before decreasing again at roughly $t/t_1 = 0.7$. The corresponding flame standoff ratio is observed to first decrease and then increase again after $t/t_1 = 0.4$, although the droplet diameter decreases continuously. It should be noted that the shadowgraph images were used to determine the droplet size and were used in combination with the OH-chemiluminescence images to calculate the resulting flame standoff ratio. Therefore, the surrounding ice layer may have obscured the actual droplet size and thus distorted the flame standoff ratio. The effects of ice formation around the burning oxygen droplet were most apparent and exhibited the greatest effect at low pressures ($p_r < 0.15$). In tests at higher pressures, no major discontinuity in the evolution of the flame diameter could be detected and the flame standoff ratio remained nearly constant, as can be seen in **Fig. 8b-c**. Also, the non-spherical shape of the droplet was observed in other experiments in the low-pressure regime up to $p_r = 0.15$. At higher pressures, ice formation and the resulting non-spherical droplet shape were less evident (**Fig. 7b-c**), but ice particles remained at the end of combustion in all experiments, similar to what can be seen in **Fig. 6**. It is expected that the decreasing flame distance, the higher flame and droplet surface temperature as well as the shorter droplet lifetimes affected the growth and the appearance of the ice layer at the droplet surface.

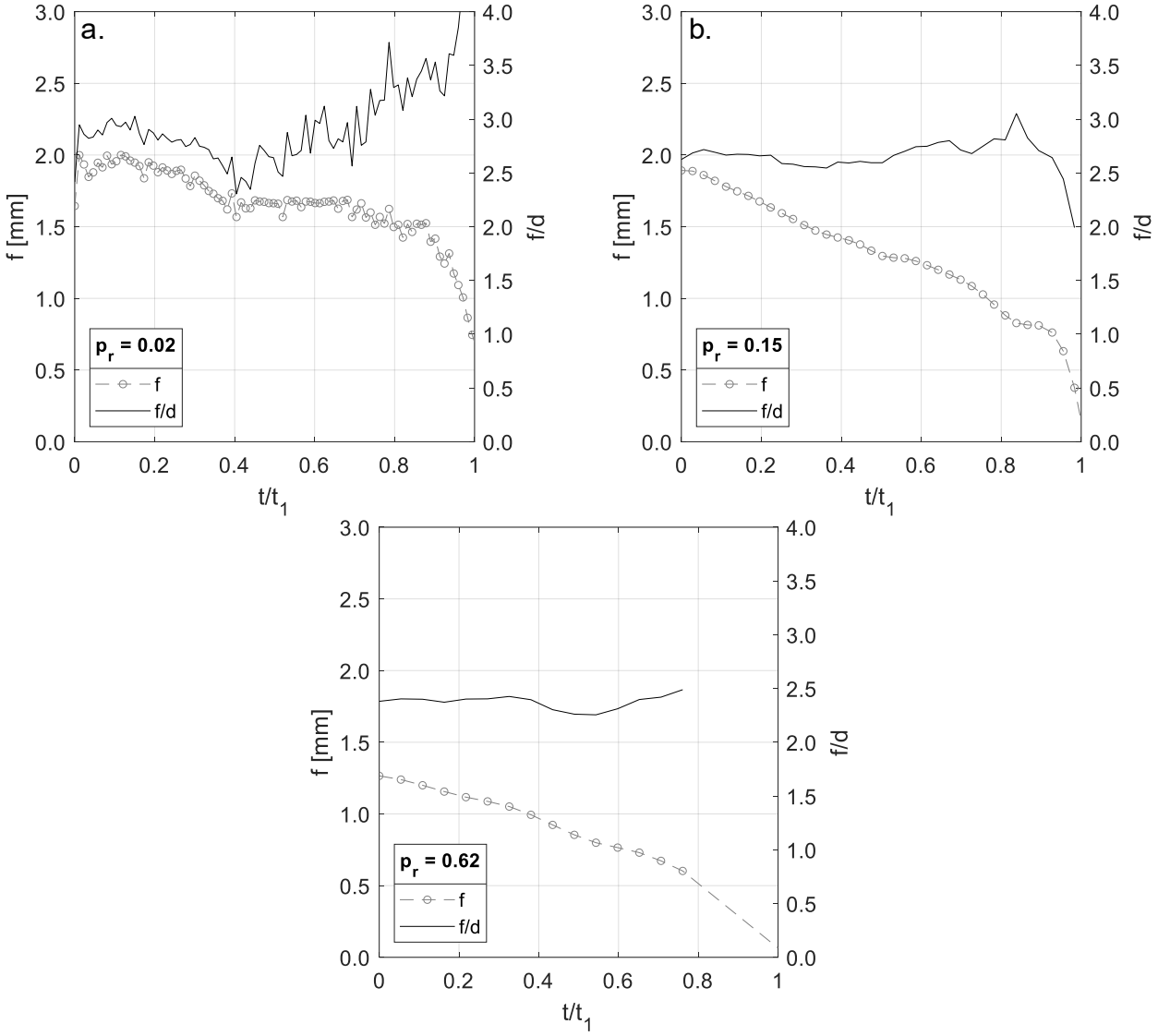

Fig. 8. Dimensionless time evolution of measured flame diameter f and calculated flame standoff ratio f/d for combustion at $p_r = 0.02$ (a), $p_r = 0.15$ (b), and $p_r = 0.62$ (c).

The effect of pressure on the flame standoff ratio in the subcritical regime is shown by the mean values between $t/t_1 = 0$ and $t/t_1 = 0.8$ as well as the corresponding standard deviation for each experiment in **Fig. 9**. Ice formation also appears to have an effect on the calculation of the flame standoff ratio due to the significant change in droplet shape at low pressures ($p_r < 0.15$). In this pressure regime, the calculated values scatter strongly over time, resulting in large standard deviations when calculating the mean value. In addition, increasing the pressure had major effect on the luminosity of the flame in both the OH-chemiluminescence and shadowgraph images, where the flame zone becomes apparent at high pressure. Another observed effect with increasing pressure was the increasing opacity of the water cloud ring outside the flame, which in some cases significantly absorbed the OH signal. Therefore, the extent of the flame at pressures $p_r > 0.15$ was determined using the shadowgraph images. The aperture, exposure and gain

settings of the different camera systems were correspondingly adjusted during the experimental campaign. This may account for some of the larger data scatter at higher pressures. Despite the scatter in the data, it appears that the ambient pressure had only a limited effect on the flame standoff ratio. With increasing pressure, the trend of the flame standoff ratio appears to decrease slightly and reaches a value of ~2.5 at a reduced pressure of 0.9.

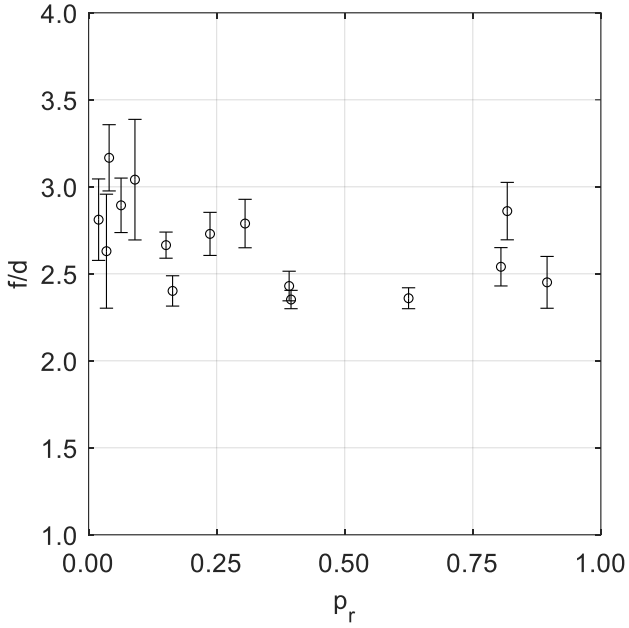

Fig. 9. Effect of reduced ambient pressure on the mean flame standoff ratio in the subcritical regime. The error bars indicate standard deviation from the mean value.

A direct comparison of the droplet diameter regression rate discussed previously at a reduced pressure of 0.02 with those at reduced pressures of 0.15 and 0.62 indicates that the regressions are much smoother at higher pressures and appear to follow the conventional d^2-law, indicating steady-state burning, as shown in **Fig. 10**. In addition, it is evident that the elapsed combustion time, normalized by the square of the initial droplet diameter, decreases slightly with increasing ambient pressure, from 187 ms/mm² ($p_r = 0.02$) to 172 ms/mm² ($p_r = 0.15$) and to 163 ms/mm² ($p_r = 0.62$), respectively. Based on the d^2-law, a burning rate constant k can be calculated for each experiment from the initial equivalent droplet diameter d_0 and the droplet lifetime after detachment from the suspender t_d according to **Eq. (1)**,

$$k = \frac{{d_0}^2}{t_d} \tag{1}$$

It is assumed for the present experimental data that the d^2-law remains valid. The ice formation, which is clearly visible in the shadowgraph images at low pressures ($p_r < 0.15$), can obscure the view of the actual droplet surface. This then apparently leads to a deviation from the linear course of the droplet diameter regression, since the ice shell is visually detected instead of the surface of the liquid droplet. Therefore, the

calculation of the burning rate constant, using **Eq. (1)**, is based on the droplet lifetime instead of the slope of the droplet regression. Since the evaluation was started only after ignition and after complete detachment of the droplet from the suspender, the transient initial phase of the droplet combustion is not included in the calculation of the burning rate constant.

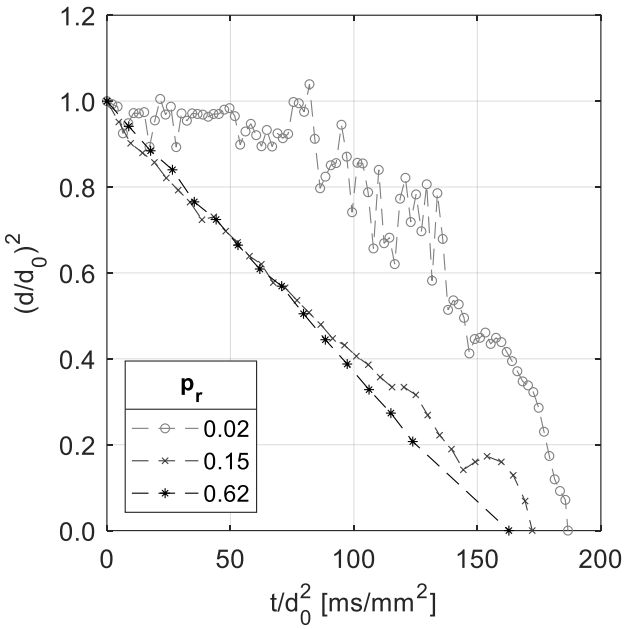

Fig. 10. Normalized time evolution of dimensionless diameter regression for different ambient pressures.

The calculated burning rate constants as a function of the reduced ambient pressure are shown in **Fig. 11**. In the subcritical pressure regime up to a pressure of $p_r = 0.4$, the burning rate constant appears to be essentially unaffected by ambient pressure, but then increases significantly when the critical pressure is approached. Above the critical pressure, the burning rate constant appears to be nearly constant with a value of ~8 mm²/s, however, the data do not extend very far into the supercritical regime due to the pressure limitation of the combustion chamber. It should be mentioned that the calculation of the burning rate constant is very sensitive to the initial droplet diameter (after detachment from the suspender occurred). Especially in the low-pressure regime, the ice layer might have obscured the view of the actual droplet surface, and thus the burning rate may have been overestimated for low-pressure experiments ($p_r < 0.15$). It is pointed out in the literature that with increasing pressure the difference between combustion lifetime and droplet lifetime increases. This is explained by the decreasing diffusion coefficient, which causes the vaporized gas to burn more slowly after reaching the droplet lifetime [22, 28]. However, in our experiments, the droplet lifetime (as indicated by the shadowgraph images) and the combustion lifetime (as indicated by the OH-imaging/shadowgraph images) were approximately the same. This is consistent with the numerical results of Lafon *et al.* [18] which indicated no significant vapor accumulation due to the low value of the flame standoff ratio, so they concluded that the droplet lifetime and the combustion lifetime are almost the

same. It should be noted, however, that at the end of the droplet lifetime, no clear distinction between liquid oxygen and water ice can be seen in the shadowgraph images. Therefore, errors in the determination of the droplet lifetime may have occurred, especially at higher pressures, such that the apparent droplet lifetime was closer to the combustion lifetime. However, due to the comparably high diffusion rate of hydrogen in oxygen and the low value of the flame standoff ratio, that error in determining the droplet lifetime is assumed to be rather small in relation to the combustion lifetime.

When comparing the results in **Fig. 11** with those from hydrocarbon combustion experiments [21-25], which based on measured combustion lifetimes, a similar progression of the burning rate constants can be seen. Based on our results, it is expected that the maximum burning rate is also reached near a reduced pressure of unity ($p_r = 1$), which is consistent with the hydrocarbon experiments (**Fig. 11**). This phenomenon can be attributed to the interaction of several thermodynamic effects. In the subcritical pressure regime, the enthalpy of vaporization takes a dominant role in the gasification of liquid oxygen [15, 16, 24]. Despite the significant decrease in the binary diffusion coefficient with increasing pressure, which would lead to a decrease in the burning rate, the decrease in the enthalpy of vaporization dominates and leads to the observed increase in the burning rate constant or decrease in the droplet lifetime.

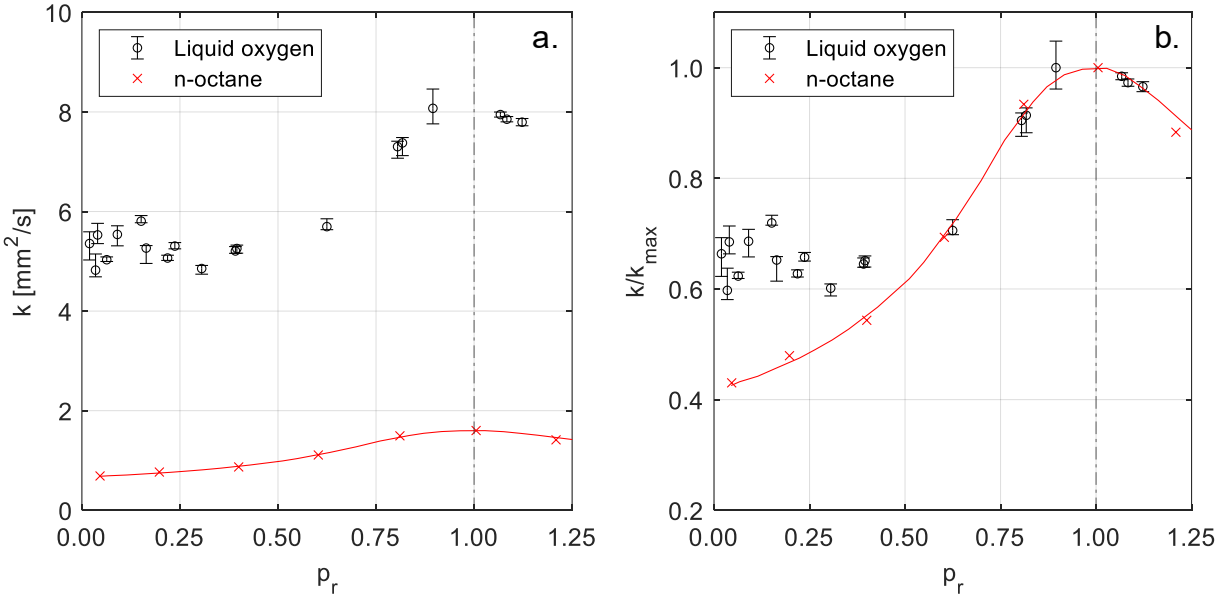

Fig. 11. Variation in burning rate constant with reduced ambient pressure for liquid oxygen and n-octane [21]. Error bars for liquid oxygen are based on the longest and shortest detected dimension of the droplet as well as on the max. time error of <500 µs. a. Absolute burning rate k. b. Normalized burning rate k/k_{max}.

The enthalpy of vaporization at the droplet surface approaches zero during the transition to the supercritical pressure regime [16]. With a further increase in ambient pressure, the diffusivity decreases further, which could cause the droplet lifetime to increase again. This is counteracted by the decreasing critical mixing

temperature with increasing pressure above the critical point [16, 17]. At a pressure above the critical point, the disappearance of the sharp distinction between gas and liquid occurs at the critical mixing temperature. Due to the pressure limitation of the combustion chamber, higher pressures could not be investigated in this study.

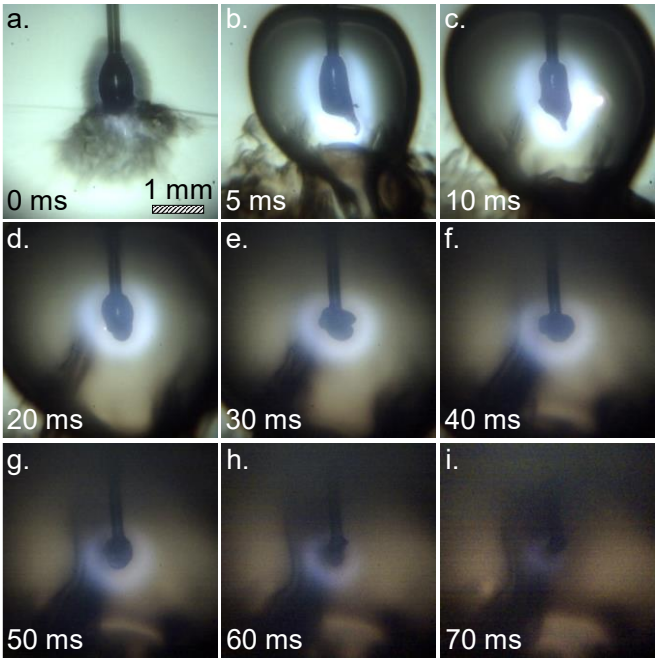

Fig. 12. a.-i. High-speed shadowgraph sequence of LOX droplet regression at an ambient pressure of $p_r = 1.07$. Brightness correction progressively increased. Ignition occurred at 0 ms (a) and induced vortices below the droplet, which affected the shape of the water cloud ring around the droplet. The shape of the droplet is distorted by these vortices and remained non-spherical throughout the combustion.

During the transition to the supercritical pressure regime, the temperature plays an essential role in reaching the supercritical state. Prior to ignition, i.e., during droplet generation, the liquid oxygen droplet was subjected to a reduced pressure greater than unity, but the temperature was 77 K ($T_r = 0.50$), well below the critical temperature of 154.6 K. Thus, the droplet behavior did not change during droplet generation and vaporization period compared to the subcritical pressure regime. After ignition, the flame presumably elevated the surface temperature of the droplet to the critical mixing temperature, resulting in a supercritical condition at the surface. However, the droplet interior may have remained liquid due to a subcritical temperature distribution [16].

One difference between subcritical and supercritical combustion is the behavior of the droplet immediately after ignition, as shown in **Fig. 12**. In the subcritical regime, the droplet changed to a spherical shape immediately after ignition, which quickly damped the oscillations triggered by the momentum resulting from the pressure spike due to the spark. In the supercritical regime, the droplet did not assume a spherical shape due to the lack of surface tension (**Fig. 12**). The damping of the perturbations introduced by the ignition seems to have been strongly weakened, so that the droplet oscillated almost until the end of the

combustion and changed shape repeatedly. For the supercritical case, the droplet confinement was presumably no longer determined by surface tension, but only by inertia [15]. However, it should be noted that, especially at the beginning of the combustion, it could be expected that the droplet did not have a homogeneous temperature distribution. Potentially, the burning droplet may have consisted of an inner liquid core, which was surrounded by a supercritical phase. With respect to the calculation of the burning rate constants (**Fig. 11**), the non-spherical shape of the droplets and the persistent oscillation at supercritical conditions might have influenced the measured values. In addition, above the critical pressure the droplet did not detach from the suspender in a controlled manner (**Fig. 12**) as in the subcritical experiments, so the equivalent droplet diameter based on the suspender-corrected droplet volume at the time of ignition was used to calculate the burning rate constant in the supercritical region. Thus, in contrast to the subcritical experiments, the possible effect of the suspender is included in the calculated burning rate constant. The described ice formation around the burning droplet, which was especially observed at low pressures, could no longer be clearly detected during combustion in the supercritical regime. However, after the end of the combustion, remaining ice particles were also visible as in subcritical conditions.

4. Conclusion

To investigate the fundamentals of hydrogen-oxygen droplet combustion as a foundation for spray combustion in rocket engines, the combustion of single liquid oxygen droplets in a quiescent hydrogen atmosphere was investigated. The experiments were conducted under microgravity conditions in the Bremen drop tower. Nineteen drop tower experiments in which ignition was successful were evaluated at a reduced ambient pressure of oxygen p_r between 0.02 and 1.12.

Especially at low pressures ($p_r < 0.15$), the shape of the droplet deviated significantly from the spherical shape during the combustion process. This could be attributed here to water ice formation near the cold droplet surface. Small oxygen vapor jets were observed to break through this ice shell. These micro-explosions could be a source of linear and angular momentum leading to the observed rotation and translation of the droplet after detachment from the suspender. In the subcritical regime, the basic combustion parameters, such as the droplet and flame zone regression or the flame standoff ratio, were determined and discussed using three different ambient pressures as examples. The droplet behavior under subcritical and supercritical conditions was qualitatively compared. Due to the vanishing of the surface tension at supercritical conditions, the droplet did not resume a spherical shape after deformation by the pressure wave of the ignition spark.

The pressure effects on combustion were studied using the flame standoff ratio and the burning rate constant. In the case of the flame standoff ratio, a slight decrease with increasing pressure was determined, but the ambient pressure appears to have only a limited effect on the flame position. However, the burning rate

constant indicates a clear dependence on the ambient pressure. In the subcritical regime, the burning rate constant is initially almost constant with increasing pressure. For $p_r > 0.15$, however, the burning rate increases significantly up to the critical pressure, which can be explained by the decrease in the enthalpy of vaporization as the dominant effect. In the supercritical pressure regime, the burning rate constant is almost constant as enthalpy of vaporization vanishes and the diffusivity decreases further. This trend was compared with published experimental results on hydrocarbon droplet combustion and found to be consistent. However, the calculation of the burning rates in this regime is subject to the effect of the suspender and the droplet surface is not spherical due to the lack of surface tension.

The experimental results provide a database on droplet combustion in the hydrogen-oxygen system. Existing or newly developed numerical (sub-)models can be compared, e.g., with the measured droplet lifetimes or the flame position to validate the numerical results. The experiments represent a first step to support the development of future detailed spray combustion models. In future experiments, the experimental setup will be improved with respect to droplet generation and diagnostics to investigate the pressure effects and the ice formation around the oxygen droplet in more detail.

Acknowledgments

We thank Günther Marks and Michael Peters (ZARM) for technical support during the experimental campaigns. This research has been funded by the German Federal Ministry for Economic Affairs and Energy through the German Space Administration (DLR) in the framework of HYDRA and HYDRA-II (grants: 50WM1645 & 50WM2065). The collaboration between ZARM (University of Bremen) and the University of Washington was supported by the US Fulbright Scholars Program.

References

[1] N. N. Smirnov, V. B. Betelin, R. M. Shagaliev, V. F. Nikitin, I. M. Belyakov, Y. N. Deryuguin*, et al.*, Hydrogen fuel rocket engines simulation using LOGOS code, Int. J. Hydrog. Energy 39 (2014) 10748-10756.

[2] V. B. Betelin, V. F. Nikitin, D. I. Altukhov, V. R. Dushin, J. Koo, Supercomputer modeling of hydrogen combustion in rocket engines, Acta Astronaut. 89 (2013) 46-59.

[3] M. Masquelet, S. Menon, Y. Jin, R. Friedrich, Simulation of unsteady combustion in a LOX-GH2 fueled rocket engine, Combust. Sci. Technol. 13 (2009) 466-474.

[4] J. C. Oefelein, V. Yang, Modeling High-Pressure Mixing and Combustion Processes in Liquid Rocket Engines, J. Propuls. Power 14 (1998) 843-857.

[5] G. A. E. Godsave, Studies of the combustion of drops in a fuel spray - the burning of single drops of fuel, Symp. (Int.) Combust. 4 (1953) 818-830.

[6] D. B. Spalding, The combustion of liquid fuels, Symp. (Int.) Combust. 4 (1953) 847-864.

[7] S. Kumagai, H. Isoda, Combustion of fuel droplets in a free falling chamber, Symp. (Int.) Combust. 6 (1957) 726-731.

[8] V. Nayagam, D. L. Dietrich, M. C. Hicks, F. A. Williams, Cool-flame extinction during n-alkane droplet combustion in microgravity, Combust. Flame 162 (2015) 2140-2147.

[9] C. Eigenbrod, V. Wagner, W. Paa, Spontaneous ignition of droplet pairs of n-Decane and n-Tetradecane in microgravity, Proc. Combust. Inst. 38 (2021) 3131-3139.

[10] M. Mikami, H. Kato, J. Sato, M. Kono, Interactive combustion of two droplets in microgravity, Symp. (Int.) Combust. 25 (1994) 431-438.

[11] A. Yang, W. Hsieh, K. Kuo, J. Brown, Evaporation of LOX under supercritical and subcritical conditions, 29th Joint Prop. Conf. (1993) AlAA 93-2188.

[12] X. Chesneau, C. Chauveau, I. Gökalp, Experiments on High Pressure Vaporization of Liquid Oxygen Droplets, 32nd Aerosp. Sci. Meeting (1994) AIAA 94-0688.

[13] J. P. Delplanque, W. A. Sirignano, Numerical study of the transient vaporization of an oxygen droplet at sub- and super-critical conditions, Int. J. Heat Mass Transf. 36 (1993) 303-314.

[14] V. Yang, N. Nienchuan, S. Jian-Shun, Vaporization of Liquid Oxygen (LOX) Droplets in Supercritical Hydrogen Environments, Combust. Sci. Technol. 97 (1994) 247-270.

[15] P. Haldenwang, C. Nicoli, J. Daou, High pressure vaporization of LOX droplet crossing the critical conditions, Int. J. Heat Mass Transf. 39 (1996) 3453-3464.

[16] V. Yang, Modeling of supercritical vaporization, mixing, and combustion processes in liquid-fueled propulsion systems, Proc. Combust. Inst. 28 (2000) 925-942.

[17] M. Oschwald, J. J. Smith, R. Branam, J. Hussong, A. Schik, B. Chehroudi*, et al.*, Injection of Fluids into Supercritical Environments, Combust. Sci. Technol. 178 (2006) 49-100.

[18] P. Lafon, M. Habiballah, Numerical analysis of droplet vaporization and burning under high-pressure conditions, 30th Joint Prop. Conf. (1994) AIAA 94-2909.

[19] P. Lafon, H. Meng, V. Yang, M. Habiballah, Vaporization of Liquid Oxygen (LOX) Droplets in Hydrogen and Water Environments under Sub- and Super-Critical Conditions, Combust. Sci. Technol. 180 (2008) 1-26.

[20] J. Daou, P. Haldenwang, C. Nicoli, Supercritical burning of liquid oxygen (LOX) droplet with detailed chemistry, Combust. Flame 101 (1995) 153-169.

[21] J. Sato, M. Tsue, M. Niwa, M. Kono, Effects of natural convection on high-pressure droplet combustion, Combust. Flame 82 (1990) 142-150.

[22] J. Sato, Studies on droplet evaporation and combustion in high pressures, 31st Aerosp. Sci. Meeting (1993) AIAA 93-0813.

[23] G. M. Faeth, D. P. Dominicis, J. F. Tulpinsky, D. R. Olson, Supercritical bipropellant droplet combustion, Symp. (Int.) Combust. 12 (1969) 9-18.

[24] B. Vieille, C. Chauveau, X. Chesneau, A. Odeïde, I. Gökalp, High-pressure droplet burning experiments in microgravity, Symp. (Int.) Combust. 26 (1996) 1259-1265.

[25] S. D. Givler, J. Abraham, Supercritical droplet vaporization and combustion studies, Prog. Energy Combust. Sci. 22 (1996) 1-28.

[26] K. Okai, O. Moriue, M. Araki, M. Tsue, M. Kono, J. Sato*, et al.*, Pressure effects on combustion of methanol and methanol/dodecanol single droplets and droplet pairs in microgravity, Combust. Flame 121 (2000) 501-512.

[27] D. L. Dietrich, P. M. Struk, M. Ikegami, G. Xu, Single droplet combustion of decane in microgravity: experiments and numerical modelling, Single droplet combustion of decane in microgravity: experiments and numerical modelling 9 (2005) 569-585.

[28] M. Mikami, O. Habara, M. Kono, J. Sato, D. L. Dietrich, F. A. Williams, Pressure Effects in Droplet Combustion of Miscible Binary Fuels, Pressure Effects in Droplet Combustion of Miscible Binary Fuels 124 (1997) 295-309.

[29] E. A. Powell, Simulation of water vapor condensation on LOX droplet surface using liquid nitrogen, NASA Technical Report (1988).

[30] R. Litchford, S.-M. Jeng, LOX vaporization in high-pressure, hydrogen-rich gas, 26th Joint Prop. Conf. (1990) AIAA 90-2191.

[31] P. Lafon, H. Meng, V. Yang, M. Habiballah, Pressure-Coupled Responses of LOX Droplet Vaporization and Combustion in High-Pressure Hydrogen Environments, Combust. Sci. Technol. 186 (2014) 1191-1208.

[32] F. Meyer, C. Eigenbrod, V. Wagner, W. Paa, J. C. Hermanson, Apparatus to investigate liquid oxygen droplet combustion in hydrogen under microgravity conditions, Rev. Sci. Instrum. 91 (2020) 105110.

[33] C. Presser, C. Avedisian, A. Gupta, H. Semerjian, Combustion of methanol and methanol/dodecanol spray flames, J. Propuls. Power 8 (1992) 553-559.

[34] P. V. C. Hough, United States Patent Office, 3069654 (1962).